Lagrangian transport by ciliary arrays

George T. Fortune [*] and Eric Lauga [†]
Department of Applied Mathematics and Theoretical Physics, Centre for Mathematical Sciences, University of Cambridge, Wilberforce Road, Cambridge CB3 0WA, United Kingdom

(Received 19 December 2024; accepted 19 October 2025; published 24 November 2025)

In many biological systems, from sinuses to airways, ciliary arrays are essential for transporting particles and bacteria. Challenging long-held assumptions, we show that the classical Eulerian view of cilia-induced flow overlooks a key feature of time-averaged transport. Using theoretical modeling and numerical simulations, we demonstrate that the drift generated by ciliary motion is not uniform, as previously predicted, but varies with distance from the ciliary surface in unexpected ways. This variation reveals drift stagnation points, offering a potential means to distinguish healthy from impaired ciliary beating and refines our understanding of fluid-driven transport.

DOI: 10.1103/t41h-gsv9

I. INTRODUCTION

Cilia are hairlike flexible appendages, two to tens of microns in length, that protrude from eukaryotic cells [1]. Their deformation, beating at frequencies of ∼10–30 Hz, generates a flow in the surrounding fluid [2,3]. This flow enables arrays of densely packed cilia to perform a variety of functions in many biological contexts [4] such as locomotion [5–7]. Of particular biological importance is the role of cilia in enabling fluid transport along biological tissues [8], be that tracheobronchial mucus in the respiratory tract (so-called mucociliary clearance) [2,9,10], ovulatory mucus and ovum in the female reproductive tract [11], epididymal fluid in the male reproductive tract [12], or cerebrospinal fluid in the brain [13]. Since insufficient fluid transport leads to illness [14], it is crucial to investigate the relationship between ciliary beating and fluid transport.

Our theoretical understanding of ciliary flows, pioneered by Taylor [15] and Blake [16], exploits the fact that cilia are densely packed in arrays and deform in a coordinated manner as metachronal waves. The individual motion of the many cilia may thus be replaced by the dynamics of an "envelope" [see the sketch in Fig. 1(a)], resulting in a continuous surface that undergoes waving deformation with both transverse and longitudinal motions [6]. This classical model was originally studied for small-amplitude waving and was extended in subsequent years in a variety of settings, including large-amplitude motion [17], the role of inertial effects [18–20], finite sheet length [21,22], sheet curvature [23], three-dimensional sheet deformation [23], or non-Newtonian fluids [8,24–27]. Placing a second envelope above the first also allows peristaltic pumping to be tackled [28,29].

One of the striking features of the envelope model for ciliary flows is the theoretical prediction that, in the small-amplitude limit relevant in the majority of experimental settings (typically, the metachronal wavelength is one to two orders of magnitude bigger than the sheet deformation amplitude), the time-averaged (Eulerian) flow induced by traveling waves in the envelope is predicted to be uniform throughout the fluid (at leading order). When the cilia undergo arbitrary surface waving, the fluid thus undergoes a time-periodic and spatially periodic motion superimposed with a uniform drift.

This prediction has served as the foundation for a substantial body of subsequent work in the literature, both theoretical and experimental. Taking the uniform drift as the quantity to be optimized, the parameter values of the waving motion that lead to the largest induced flow for a fixed amount of energy expended by the cilia can thus be derived [2,30].

With a ciliated organism seen effectively as a ciliary carpet, changing reference frames to one in which the far field is at rest, the uniform drift becomes precisely the swimming speed of the organism. Hence, this prediction can also be used to probe a large variety of swimming optimization questions [31], e.g., the geometric shape of an axisymmetric microswimmer that maximizes its swimming speed [32] or the density of cilia that optimizes propulsion efficiency [33].

In mucociliary transport, the key measurable quantity is mucus transport velocity, typically obtained by tracking the time a tracer takes to move a fixed horizontal distance (a time-averaged drift velocity) [34–37]. For this to be well defined, tracers must drift horizontally at a constant speed, independent of position. This assumption (implicitly) comes from theory, which predicts a constant horizontal Eulerian drift velocity. However, experiments measure not the Eulerian but the *Lagrangian* drift velocity, which can differ; in particular, the latter can have a value that depends on the vertical distance to the cilia. Experimentally, three different types of tracers

[*]Contact author: gtf22@damtp.cam.ac.uk
[†]Contact author: e.lauga@damtp.cam.ac.uk

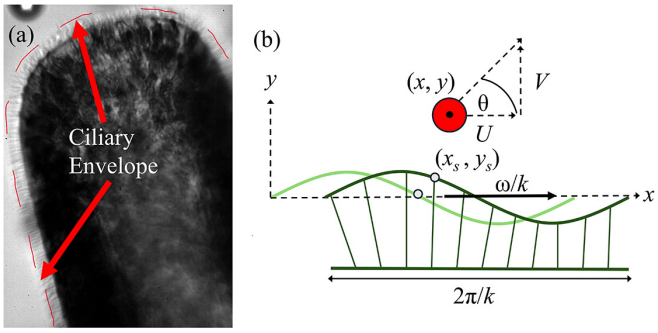

FIG. 1. Envelope of ciliary arrays. (a) Photograph of the ciliary envelope on an acoel, the plant-animal worm *Symsagittifera roscoffensis* (image credit George T. Fortune and Goldstein Laboratory). (b) Schematic of a particle, instantaneously moving at an angle θ relative to a beating ciliary carpet, whose tips can be represented as a waving sheet of wavelength $2\pi/k$, frequency ω, and wave speed ω/k that generates a fluid flow (U, V). Considering a reference frame in which the carpet centerline is stationary, x and y are the laboratory frame coordinates of the particle, while x_s and y_s denote the material points on the carpet.

have been used: fine colloids (e.g., India ink [34]), powders (e.g., charcoal [35] or polymer beads [36]), or floating debris tracked on the mucus surface [37]. Each probes a different quantity, yielding different mucus transport velocities for the same system. To our knowledge, Lagrangian transport in ciliary arrays has received little study, a gap this manuscript aims to fill.

In this paper, we thus go back to first principles and show that applying the classical Eulerian prediction to the transport of suspended bodies in the cilia-driven fluid flow, such as passive particles or nonmotile bacteria, leads to incorrect predictions for the time-averaged transport. Combining numerical simulations with multiple-scale asymptotics, we reveal that the Lagrangian transport of suspended particles is indeed not uniform in the fluid, but instead depends on the distance to the ciliary envelope in unexpected ways. This discovery reveals drift stagnation points, providing a way to distinguish healthy from impaired ciliary beating patterns, which we show is directly applicable to experimental data, and refines our understanding of fluid-driven transport.

II. MODELING CILIA FLOWS: TAYLOR'S WAVING SHEET

A. Continuum model: Ciliary array and flow

In this section, we outline the canonical Taylor waving sheet model that we will investigate in the rest of the paper [15]. Consider a continuous array of cilia beating in the $x-y$ plane. As illustrated in Fig. 1(b), material points on the ciliary envelope (x_s, y_s) are assumed to undergo a prescribed sinusoidal waving motion characterized through the relation

$$x_s = x + A\cos(kx - \omega t - \phi),$$
$$y_s = B\sin(kx - \omega t), \tag{1}$$

with wavelength $2\pi/k$, frequency ω, and wave speed ω/k. Note that with this formulation, the trajectories of material points are ellipses in (x, y) space . The transverse and longitudinal motions of points on this carpet have amplitudes A and B, respectively, with relative phase difference ϕ. We scale length scales with k^{-1}, scale timescales with ω^{-1}, and set $a = Ak/\epsilon$ and $b = Bk/\epsilon$, where the nondimensional amplitude ϵ satisfies

$$\epsilon = \sqrt{A^2 + B^2}/k^{-1} \ll 1. \tag{2}$$

The nondimensionalized coordinates of points on the ciliary carpet are thus given by

$$x_s = x + \epsilon a\cos(x - t - \phi),$$
$$y_s = \epsilon b\sin(x - t), \tag{3}$$

with $a^2 + b^2 = 1$. This ciliary beating induces a velocity field in the fluid. The evolution equations for this velocity field are too mathematically complex to admit closed analytic solutions for general ϵ. We follow the classical approach by restricting to the cases where ϵ is small [16]. Order of magnitude estimates for k^{-1}, ω, A, and B for typical epithelial cilia carpets are given by

$$k^{-1} \approx 10\ \mu\text{m}, \quad A, B \approx 1\ \mu\text{m}, \quad \omega \approx 10^2\ \text{s}^{-1}. \tag{4}$$

With these values, we obtain $\epsilon = \mathcal{O}(10^{-1})$; i.e., experimentally, we are indeed in the regime where $\epsilon \ll 1$. In this limit, through an expansion of the governing equations in terms of ϵ, we may derive expressions prescribing the evolution of a material point $(x(t), y(t))$ in the flow up to and including the $\mathcal{O}(\epsilon^2)$ terms. In particular, define the streamfunction ψ as satisfying $U = \partial\psi/\partial y$ and $V = -\partial\psi/\partial x$. From Refs. [6,8], ψ can be expressed as a series expansion in terms of ϵ as

$$\begin{aligned}\psi =\ & \epsilon[aye^{-y}\sin(x - t - \phi) + b(1 + y)e^{-y}\sin(x - t)] \\ & + \epsilon^2\Big[-ye^{-2y}(ab\sin\phi + a^2\cos\phi\sin\phi)\sin 2(x - t) \\ & + \frac{ye^{-2y}}{2}(a^2\sin^2\phi - a^2\cos^2\phi - 2ab\cos\phi - b^2) \\ & \times \cos 2(x - t) \\ & + \frac{y}{2}(b^2 + 2ab\cos\phi - a^2)\Big] + \mathcal{O}(\epsilon^3).\end{aligned} \tag{5}$$

Hence, U and V become

$$\begin{aligned}U =\ & \epsilon a(1 - y)e^{-y}\sin(x - t - \phi) - \epsilon bye^{-y}\sin(x - t) \\ & + \frac{\epsilon^2(1 - 2y)e^{-2y}}{2}\cos 2(x - t) \\ & \times (a^2\sin^2\phi - a^2\cos^2\phi - 2ab\cos\phi - b^2) \\ & - \epsilon^2(1 - 2y)e^{-2y}(ab\sin\phi + a^2\cos\phi\sin\phi)\sin 2(x - t) \\ & + \frac{\epsilon^2}{2}(b^2 + 2ab\cos\phi - a^2) + \mathcal{O}(\epsilon^3)\end{aligned} \tag{6}$$

and

$$\begin{aligned}V =\ & -\epsilon b(1 + y)e^{-y}\cos(x - t) - \epsilon aye^{-y}\cos(x - t - \phi) \\ & + 2\epsilon^2 ye^{-2y}(ab\sin\phi + a^2\cos\phi\sin\phi)\cos 2(x - t) \\ & + \epsilon^2 ye^{-2y}\sin 2(x - t) \\ & \times (a^2\sin^2\phi - a^2\cos^2\phi - 2ab\cos\phi - b^2) + \mathcal{O}(\epsilon^3).\end{aligned} \tag{7}$$

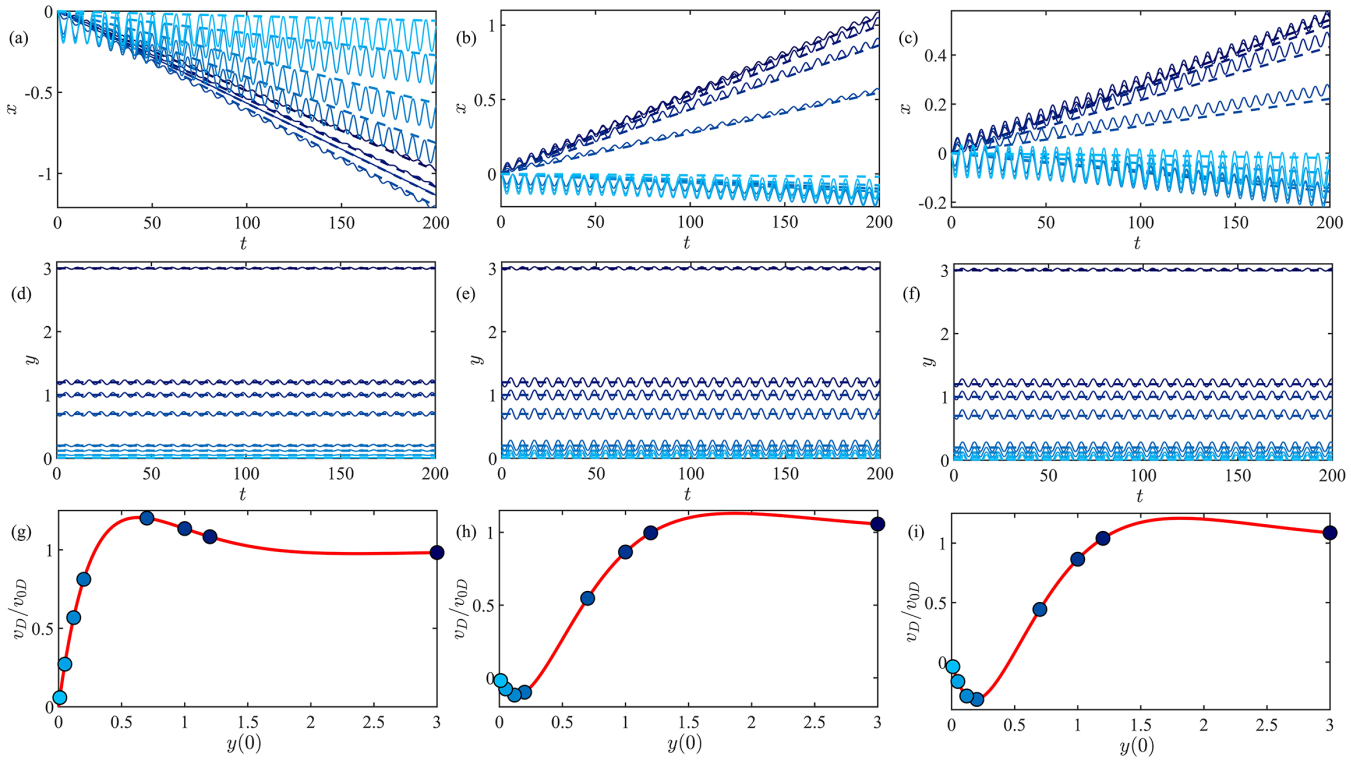

FIG. 2. Lagrangian trajectories of particles transported by ciliary arrays. Numerical solutions (solid curves) and asymptotic approximations for the drift (dashed lines), plotting x and y as a function of time t for $y(0) \in (0.01, 0.05, 0.12, 0.2, 0.7, 1, 1.2, 3)$ and a range of values for (a, ϕ) with $x(0) = 0$ and $\epsilon = 0.1$. Darker blue indicates larger $y(0)$. All quantities (x, y, t) have been nondimensionalized with respect to the scalings given in Sec. II. (a), (d), (g) $a = 1, \phi = 0$. (b), (e), (h) $a = 1/\sqrt{2}, \phi = 0$. (c), (f), (i) $a = 1/\sqrt{2}, \phi = \pi/3$. (g), (h), (i) The normalized drift velocity v_D/v_{0D} as a function of $y(0)$ (red line), where v_{0D} is the Eulerian prediction from Eq. (8). The $y(0)$ values used in the other figures are indicated by colored blue dots.

This is typically where the standard modeling approach ends, with the calculation of the induced Eulerian flow, or Eulerian drift. It occurs only in the x direction and can be obtained either by computing the time average of Eqs. (6) and (7) or by calculating the instantaneous Eulerian velocity in the far field ($y \to \infty$), both of which lead to a steady uniform drift velocity v_{0D} along x with

$$v_{0D} = \frac{\epsilon^2}{2}(b^2 + 2ab\cos\phi - a^2). \tag{8}$$

B. Lagrangian transport: Model

If instead we are interested in the time-varying transport of a particle, its position (x, y) evolves according to the governing equations

$$\begin{aligned}\frac{\partial x}{\partial t} &= \epsilon a(1-y)e^{-y}\sin(x-t-\phi)\\ &\quad - \epsilon b y e^{-y}\sin(x-t) + \frac{\epsilon^2}{2}(b^2 + 2ab\cos\phi - a^2)\\ &\quad - \epsilon^2(1-2y)e^{-2y}(ab\sin\phi + a^2\cos\phi\sin\phi)\\ &\quad \times \sin 2(x-t) + \frac{\epsilon^2 e^{-2y}}{2}(1-2y)\cos 2(x-t)\\ &\quad \times (a^2\sin^2\phi - a^2\cos^2\phi - 2ab\cos\phi - b^2)\\ &\quad + \mathcal{O}(\epsilon^3),\end{aligned} \tag{9a}$$

$$\begin{aligned}\frac{\partial y}{\partial t} &= -\epsilon b(1+y)e^{-y}\cos(x-t) - \epsilon a y e^{-y}\cos(x-t-\phi)\\ &\quad + 2\epsilon^2 y e^{-2y}(ab\sin\phi + a^2\cos\phi\sin\phi)\cos 2(x-t)\\ &\quad + \epsilon^2 y e^{-2y}\sin 2(x-t)\\ &\quad \times (a^2\sin^2\phi - a^2\cos^2\phi - 2ab\cos\phi - b^2) + \mathcal{O}(\epsilon^3).\end{aligned} \tag{9b}$$

C. Lagrangian transport: Computational results

This Lagrangian system of equations in Eq. (9) is straightforward to solve numerically for a range of initial conditions and parameter values for ϵ, for example, using matlab [38]. In Fig. 2, we present results for three representative points in the (a, θ) phase plane: the base case with only transverse motion $a = 1, \phi = 0$ in the left column of Fig. 2 [i.e., panels (a), (d), and (g)], both transverse and longitudinal motions but no phase difference $a = 1/\sqrt{2}, \phi = 0$ in the middle column of Fig. 2 [panels (b), (e), and (h)], and both transverse and longitudinal motions with a phase difference $a = 1/\sqrt{2}, \phi = \pi/3$ in the right column of Fig. 2 [panels (c), (f), and (i)].

In all these cases, we plot the evolution of both the horizontal displacement $x(t)$ [first row, i.e., Figs. 2(a)–2(c)] and the vertical displacement $y(t)$ [second row, i.e., Figs. 2(d)–2(f)] as functions of time t for $\epsilon = 0.1$, shown as solid lines starting from $x(0) = 0$ and a range of initial heights $y(0)$ above the

beating cilia envelope. Here, darker blue corresponds to larger values of $y(0)$.

It is evident from these plots that the transported particles follow trajectories characterized by a superposition of a high-frequency periodic orbit and a slower drift in the horizontal x direction. We therefore plot in the third row, i.e., Figs. 2(g)–2(i), the net drift velocity in the x direction, defined as the time-averaged velocity of the transported particle, normalized by the Eulerian value v_{0D} from Eq. (8).

Strikingly, we obtain the result that the net drift experienced by the particles is nonmonotonic in the initial distance $y(0)$ from the ciliary array. This stands in contrast to the classical Eulerian picture in the literature, which predicts uniform drift [Eq. (8)]. Moreover, we observe from Figs. 2(g)–2(i) that the drift can unexpectedly change sign. Suitable choices of the waving amplitudes and phases (a, ϕ) can therefore induce recirculation; i.e., there exist values of $y(0)$ for which the drift is negative, and others for which it is positive.

The nonmonotonicity and possibility of recirculation in the Lagrangian drift reveal an intriguing set of dynamics, which we now proceed to explore mathematically.

III. LAGRANGIAN TRANSPORT: METHOD OF MULTIPLE SCALES

Why are the Lagrangian trajectories so different from the average flow? Fundamentally, the time-averaged transport by the unsteady flow is not the same as the transport by the time-averaged flow (which is uniform), due to the nonlinear nature of the transport equations. We can rationalize this quantitatively by noting that the system is clearly characterized by two different timescales: a fast scale responsible for the oscillations (which is $\mathcal{O}(1)$ in the dimensionless problem) and a slow timescale governing the horizontal drift (which is $\mathcal{O}(\epsilon^2)$). The presence of two timescales is evident in the time-varying plots of Fig. 2 (top two rows).

We propose here that the system may be analyzed using the method of multiple scales [39] to derive asymptotic approximations for these trajectories valid in the limit $\epsilon \ll 1$. This general method is applicable to a wide range of problems that have two physical processes, each with their own scales and with the two processes acting simultaneously. Originally, it was applied to classic dynamical systems such as the Van der Pol oscillator [40,41] and the Mathieu equation [39]. More recently, it has been employed very successfully to make analytical progress in a large variety of problems in biological physics concerning microswimmers where rapid oscillatory motion over short timescales gives way to larger-scale emergent trajectories over long timescales [42–47].

A. Asymptotic calculation at small amplitude, $\epsilon \ll 1$

To compute the trajectories using the method of multiple scales, we formally express x and y as functions of both t and the slow timescale $T = \epsilon^2 t$, so that

$$\frac{d}{dt} \to \frac{\partial}{\partial t} + \epsilon^2 \frac{\partial}{\partial T}. \tag{10}$$

We then expand x, y as series expansions in powers of ϵ as

$$x = x_0 + \epsilon x_1 + \epsilon^2 x_2 + \cdots, \tag{11a}$$
$$y = y_0 + \epsilon y_1 + \epsilon^2 y_2 + \cdots \tag{11b}$$

and proceed to solve the system order by order.

At $\mathcal{O}(1)$, Eq. (9) becomes

$$\frac{\partial x_0}{\partial t} = \frac{\partial y_0}{\partial t} = 0, \tag{12}$$

i.e., x_0 and y_0 are functions of the slow timescale T only. Next, taking Eq. (9) at $\mathcal{O}(\epsilon)$ and then integrating with respect to t gives

$$x_1 = a(1-y_0)e^{-y_0}\cos(x_0 - t - \phi) - by_0 e^{-y_0}\cos(x_0 - t) + g_1(T), \tag{13a}$$
$$y_1 = ay_0 e^{-y_0}\sin(x_0 - t - \phi) + b(1+y_0)e^{-y_0}\sin(x_0 - t) + g_2(T), \tag{13b}$$

where g_1 and g_2 are independent of t, i.e., just functions of T.

At $\mathcal{O}(\epsilon^2)$, Eq. (9) becomes

$$\begin{aligned}\frac{\partial x_2}{\partial t} + \frac{\partial x_0}{\partial T} &= ax_1(1-y_0)e^{-y_0}\cos(x_0 - t - \phi) - ay_1 e^{-y_0}(2-y_0)\sin(x_0 - t - \phi) - by_1 e^{-y_0}(1-y_0)\sin(x_0 - t)\\ &\quad - by_0 x_1 e^{-y_0}\cos(x_0 - t) + \frac{1}{2}(b^2 + 2ab\cos\phi - a^2) + \frac{1}{2}e^{-2y_0}(1-2y_0)\cos 2(x_0 - t)\\ &\quad \times (a^2\sin^2\phi - a^2\cos^2\phi - 2ab\cos\phi - b^2) - (1-2y_0)e^{-2y_0}\sin 2(x_0 - t)(ab\sin\phi + a^2\cos\phi\sin\phi),\end{aligned} \tag{14a}$$

$$\begin{aligned}\frac{\partial y_2}{\partial t} + \frac{\partial y_0}{\partial T} &= ay_0 x_1 e^{-y_0}\sin(x_0 - t - \phi) - ay_1(1-y_0)e^{-y_0}\cos(x_0 - t - \phi)\\ &\quad + by_0 y_1 e^{-y_0}\cos(x_0 - t) + bx_1(1+y_0)e^{-y_0}\sin(x_0 - t) + y_0 e^{-2y_0}\sin 2(x_0 - t)\\ &\quad \times (a^2\sin^2\phi - a^2\cos^2\phi - 2ab\cos\phi - b^2) + 2y_0 e^{-2y_0}\cos 2(x_0 - t)(ab\sin\phi + a^2\cos\phi\sin\phi).\end{aligned} \tag{14b}$$

Now, note that x_1 and y_1 are periodic in a 2π interval of t. To ensure the asymptotic consistency of the expansions for x and y when $T = \mathcal{O}(1)$, we further assume periodicity in a 2π interval of t of x_2 and y_2. Hence, integrating between 0 and 2π with respect to t gives

$$\frac{\partial x_0}{\partial T} = \frac{e^{-2y_0}}{2}((a^2 - b^2 - 2ab\cos\phi) - 4y_0(a^2 + ab\cos\phi) + 2y_0^2(a^2 + b^2 + 2ab\cos\phi)) - \frac{1}{2}(a^2 - b^2 - 2ab\cos\phi). \quad (15a)$$

$$\frac{\partial y_0}{\partial T} = 0, \quad \Longrightarrow y_0 \text{ is constant.} \quad (15b)$$

Putting this all together, we thus obtain fast oscillations on a timescale t coupled with a slower drift with velocity v_D on a timescale T, where v_D satisfies

$$v_D = \frac{\epsilon^2 e^{-2y_0}}{2}[(a^2 - b^2 - 2ab\cos\phi) - 4y_0(a^2 + ab\cos\phi) + 2y_0^2(a^2 + b^2 + 2ab\cos\phi)] - \frac{\epsilon^2}{2}(a^2 - b^2 - 2ab\cos\phi), \quad (16)$$

recalling that by definition $a^2 + b^2 = 1$. Note that the Lagrangian drift in Eq. (16) is given by the Eulerian drift plus a term that exponentially decays with the distance away from the cilia carpet y_0.

B. Comparison with computational results

The asymptotic predictions for the drift in Eq. (16) are plotted in Fig. 2 as dashed lines (darker blue corresponds to larger values of $y(0)$), showing an excellent agreement with the computational results from Sec. II C. We further show in Figs. 2(g)–2(i) the theoretical asymptotic prediction for v_D as a function of $y(0)$, normalized by the Eulerian prediction (v_{0D}), as red solid lines. Here, also we obtain strong agreement with the drift computed numerically, confirming in particular that the Lagrangian drift is not monotonic and is asymptotically equal to the Eulerian prediction only in the far field ($y \gg 1$, $v_D/v_{0D} \to 1$).

C. Error estimates for asymptotic results

The asymptotic calculations that culminate in Eq. (16) are only strictly valid in the asymptotic limit $\epsilon \ll 1$, so we next seek to evaluate quantitatively how well the agreement seen in Fig. 2 extends on a wide range of parameter values. It is readily apparent that the error is not just a function of ϵ but depends on all parameters (a, ϕ, y_0); indeed, the time-varying curves in Fig. 2(e) show more deviation from the theory than those in Fig. 2(a).

Mathematically, the asymptotic results are the leading-order $\mathcal{O}(\epsilon^2)$ contribution to the Lagrangian transport, with subsequent correction terms being $\mathcal{O}(\epsilon^3)$. To investigate the magnitude of the actual error, for given values of (a, ϕ, ϵ) we define the quantity Δv_D as the maximum error across a range of values for y_0, i.e.,

$$\Delta v_D = \max_{\{y_0 \in Y\}} |v_{\text{Dasymp}} - v_{\text{Dnum}}|, \quad (17)$$

where $v_{\text{Dasymp}} = v_{\text{Dasymp}}(a, \phi, \epsilon, y_0)$ and $v_{\text{Dnum}} = v_{\text{Dnum}}(a, \phi, \epsilon, y_0)$ are, respectively, the asymptotic and numerical approximations for the drift velocity, while $Y = [0.1, 0.3, 0.5, 0.7, 0.9]$ is a representative set of $y(0)$ values. We then plot in Fig. 3 the dimensionless value $\Delta v_D/\epsilon^3$ as a function of ϵ for $a = b = 1/\sqrt{2}$ and a range of phases ϕ.

We note first that all curves flatten out as ϵ becomes small; i.e., the absolute error does indeed decay like ϵ^3 leading to a relative error of $\mathcal{O}(\epsilon)$. Next, even for ϵ up to 0.5, the absolute error is still $\mathcal{O}(\epsilon^3)$. Furthermore, perhaps surprisingly, the prefactor remains below 0.1 when *a priori* we would expect it to be $\mathcal{O}(1)$. Hence, the asymptotic analysis remains quantitatively accurate with a relative error of $\mathcal{O}(\epsilon)$ up to the experimental limit with $\epsilon = \mathcal{O}(0.1)$.

IV. LAGRANGIAN DRIFT: STAGNATION POINTS

At the end of Sec. II C, we noted that the nonmonotonicity of the Lagrangian drift seen in Fig. 2 (bottom) can be interpreted as the existence of recirculation. In other words, there exist stagnation points in the transport: spatial locations $y_0 > 0$, at which there is zero drift, $v_D(a, \phi, y_0) = 0$, for suitable choices of the waving sheet parameters (a, ϕ). In this section, we further quantify this numerical observation by exploring our asymptotic results.

A. Illustration of drift velocity stagnation points

Equating our asymptotic expression for the drift velocity given in Eq. (16) to zero gives an implicit equation for y_0 as

$$(e^{2y_0} - 1)(a^2 - b^2 - 2ab\cos\phi) = 2y_0^2(a^2 + b^2 + 2ab\cos\phi) - 4y_0(a^2 + ab\cos\phi), \quad (18)$$

where we recall that due to nondimensionlization $a^2 + b^2 = 1$. We plot in Fig. 4(a) the numerically calculated values for y_0 in Eq. (18) as a function of ϕ for three values of a: when transverse motion dominates longitudinal motion ($a = 0.8, b = 0.6$), when transverse and longitudinal motions

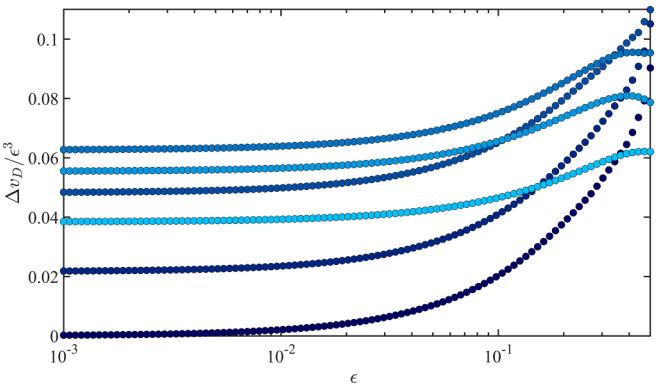

FIG. 3. Drift error estimates. The error metric Δv_D scaled by ϵ^3 is plotted as a function of ϵ for a range of values of ϕ of the form $\phi = n/20$, where n is a positive integer less than 20 and $a = 1/\sqrt{2}$. Darker blue curves indicate smaller values of ϕ.

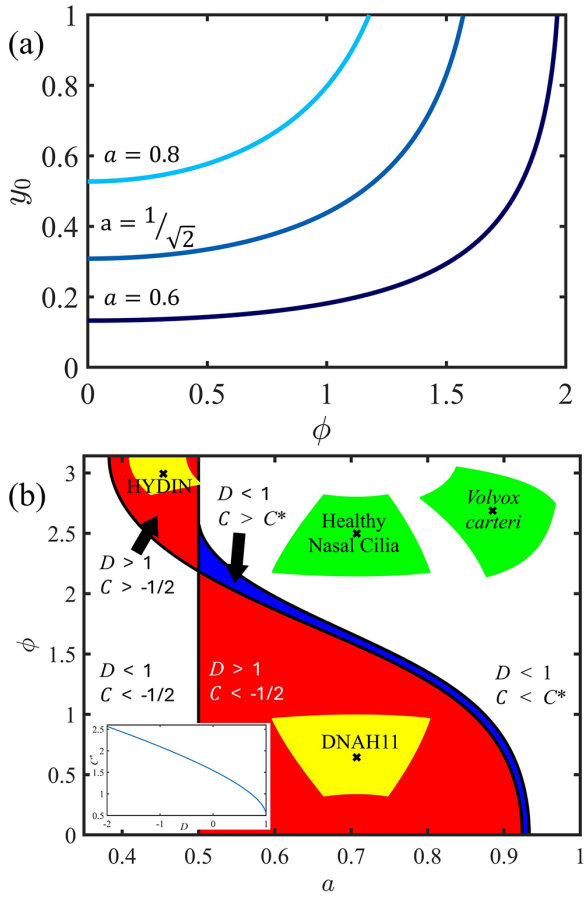

FIG. 4. Drift velocity stagnation points. (a) The vertical location of the drift stagnation point y_0 (i.e., $v_D(y_0) = 0$ when we are in a regime where such a unique y_0 exists) plotted as a function of ϕ for $a \in (0.6, 1/\sqrt{2}, 0.8)$. Darker blue curves denote smaller values of a. (b) Phase diagram plotting the regions of (a, ϕ) space where there are two (blue), one (red), or no location (white) in the fluid where the horizontal drift velocity is zero. Green (healthy cilia: *Volvox carteri* and healthy nasal cilia) and yellow regions (unhealthy cilia: nasal cilia with a mutation in either the HYDIN or DNAH11 protein) indicate the estimated locations of real ciliated systems. Inset: $C^\star$ plotted as a function of D.

are equal ($a = b = 1/\sqrt{2}$), and when longitudinal motion dominates transverse motion ($a = 0.6, b = 0.8$).

Recalling from Eq. (4) that lengths have been nondimensionlized by k^{-1} (which is on the order of 10 μm for typical epithelial cilia carpets, while the transverse and longitudinal amplitudes of points on the carpet A and B are on the order of 1 μm), we see that, reassuringly, the stagnation points are always away from the near-envelope region.

B. Wave parameters with stagnation points

In order to mathematically locate the parameters (a, ϕ) in phase plane where Eq. (18) has solutions, we see that the equation is equivalent to requiring that $y > 0$ satisfies

$$e^y - 1 = Dy + Cy^2, \tag{19}$$

where we have defined $y = 2y_0$ and where C and D are given by

$$C = \frac{1 + 2ab\cos\phi}{2(a^2 - b^2 - 2ab\cos\phi)}, \tag{20a}$$

$$D = \frac{-2(a^2 + ab\cos\phi)}{a^2 - b^2 - 2ab\cos\phi}. \tag{20b}$$

This reformulation recasts this problem as finding intersection points between a quadratic $(Dy + Cy^2)$ and an exponential $(e^y - 1)$. Both curves pass through the origin. If the quadratic grows initially faster than the exponential, eventually the exponential catches up and then keeps on growing faster, resulting in a single intersection point. Since Taylor expanding yields $e^y - 1 = y + y^2/2 + \cdots$, this is equivalent to mathematically imposing that $D > 1$, i.e.,

$$\frac{4a^2 - 1}{1 - 2a^2 + 2a\sqrt{1 - a^2}\cos\phi} > 0. \tag{21}$$

Hence, the region corresponding to there being a unique stagnation point is bounded between the curves $a = 1/2$ and $\phi = \arccos(1 - 2a^2)/(2a\sqrt{1 - a^2})$.

Alternatively, if the quadratic does not grow initially faster than the exponential ($D < 1$), there are two possible cases. For fixed D, if $C < C^\star$ for some critical value $C^\star = C^\star(D)$, the exponential always grows faster than the quadratic leading to no intersection points. Alternatively, when $C > C^\star$, the quadratic overtakes the exponential and then the exponential reovertakes the quadratic, leading to exactly two intersection points. Mathematically, at the critical point $C = C^\star(D)$, the two curves are tangent at their intersection point. Hence, there exists a $y_D = y_D(D) > 0$, where

$$\left\{\begin{array}{c} e^{y_D} - 1 = Dy_D + C^\star(y_D)^2, \\ e^{y_D} = D + 2C^\star y_D, \end{array}\right\} \Longrightarrow$$

$$e^{y_D}\left(\frac{2}{y_D} - 1\right) - \frac{2}{y_D} - D = 0, \Longrightarrow$$

$$e^{y_D} + D = (2 + 2D)\left(\frac{1}{2 - y_D}\right). \tag{22}$$

However, since Eq. (22) can be formulated as locating the intersection points y_D of an exponential and a hyperbola, this cannot be solved analytically. Instead, for any given D, we may numerically solve Eq. (22) using matlab [38].

We plot in Fig. 4(b) the complete phase portrait in (a, ϕ) space with the regions with zero, one, and two stagnation points colored in white, red, and blue, respectively. We also include, as an inset, the dependence of $C^\star$ with D. In the next section, we investigate the biological relevance of these stagnation points in ciliary flows.

V. COMPARISON WITH EXPERIMENTAL CILIARY BEATING PATTERNS

A natural next step in biological fluid mechanics, once theoretical modeling progress has been made, is to gain biological insight through comparison with experimental data. In this section, we perform this comparison by defining the ciliary envelope of the Taylor beating sheet model as the surface produced by coarse graining the set of cilia centers of mass,

approximating the trajectory of the center of mass of a cilium as an ellipse. This allows us to then estimate values for the Taylor beating sheet parameters a and ϕ for four experimental ciliated systems. By identifying where these experimental systems sit on the phase diagram in Fig. 4, we can then propose a link between the existence of stagnation points and unhealthy ciliary beating patterns.

A. Ciliary envelope approximation

Fundamentally, Taylor's beating sheet model is an approximation, reducing the combined flow of many deformable cilia to a single ciliary envelope. Here, we explore how this envelope should be positioned when analyzing real ciliated systems.

The standard canonical method is to draw the continuous surface of the envelope across the tips of the cilia [6], following the approach of Blake, who first applied Taylor's beating sheet to a planar ciliary array [16]. However, not in that work, or to the best of our knowledge anywhere in the literature, has it been quantitatively justified why taking the ciliary tips is the most accurate approximation compared to taking another point on the cilia, such as the center of mass.

Clearly, this question merits careful further study in its own right, which is beyond the scope of this paper. Here, we would like to argue that fitting through the centers of mass ought to give at least as accurate a fit as fitting through the tips, and probably even a better one. Thinking of cilia as chains of point forces, it is physically intuitive for the effective average effect of the chain in the far field to arise from the center of the cilium rather than from its tip. Indeed, past investigations of a single cilium beating in isolation have concluded that the best point-force approximation for the flow field is to place the force at the center of mass of the cilium [48–51]. Recently, a study of the ciliated embryo of the amphibian *Xenopus laevis*, which has a sparse mosaic pattern of dense cilia bundles surrounded by nonciliated goblet cells, found that the flow generated by any particular bundle can be represented by a single Stokeslet positioned below the ciliary tips inside the bundle [52]. Further, numerical work modeling ciliary arrays often utilize the method of regularized singularities, approximating the flow generated by each cilium by that of a point force placed somewhere between the base and the tips; for example, work in Ref. [53] places the point forces at a height $0.7L$ above the base, where L is the length of a cilium.

Hence, in what follows, we fit the ciliary envelope to centers of mass rather than to tips. It is worth noting that, by definition, the way the Taylor beating sheet is constructed through sinusoidal functions in Eq. (1) implies that points on the envelope move in elliptical trajectories. Experimental data show that cilia centers of mass fit elliptical paths more closely than cilia tips, leading to a more accurate mapping and thus a better approximation.

B. Trajectory of cilium center of mass

We now model the trajectory of the center of mass of a cilium. We illustrate in Fig. 5(a) the beating of a single cilium from a somatic cell of *Volvox carteri*, showing the characteristic two-stroke motion described in Ref. [48]. In particular,

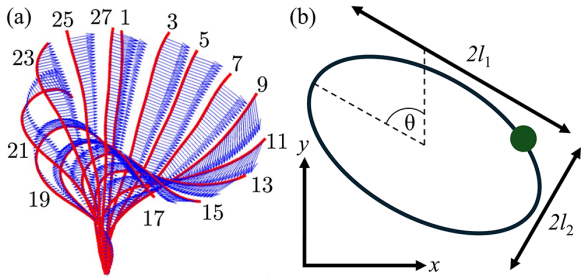

FIG. 5. Beating of a single cilium. (a) Diagram of a single cilium (flagellum) from a somatic cell of *Volvox carteri* deforming in a two-stroke motion. Arrows show the instantaneous velocity distribution along the flagellum, indexed by frame number with frame rate 1000 fps. Adapted from Ref. [48], with permission. (b) Schematic of a model of the motion of the center of mass of a cilium, utilizing an elliptical trajectory with minor axis l_2 and major axis l_1 inclined by an angle θ in the (x, y) plane.

note that the forward stroke is faster than the recovery stroke. As illustrated in Fig. 5(b), we next utilize the classical approximation from the literature [48–51], modeling the trajectory as traveling along an ellipse of minor and major axes l_2 and $l_1 > l_2$ inclined at an angle θ to the vertical.

For completeness, we note that the cited examples from the literature concern healthy ciliary beating patterns. We make below the further assumption that this elliptical orbit model also holds as a leading-order approximation for unhealthy beating patterns. We are not aware of past studies examining trajectories for unhealthy cilia, so we view this assumption as a reasonable first step. A more detailed investigation into such cases would represent a possible direction for future work.

Mathematically, coordinates for the center of mass of the cilium (x_s, y_s) can be written as

$$\begin{aligned}\begin{pmatrix} x_s \\ y_s \end{pmatrix} &= \begin{pmatrix} x \\ 0 \end{pmatrix} + \begin{pmatrix} \cos\theta & -\sin\theta \\ \sin\theta & \cos\theta \end{pmatrix} \begin{pmatrix} l_2 \cos(kx - \omega t) \\ l_1 \sin(kx - \omega t) \end{pmatrix} \\ &= \begin{pmatrix} x + l_2 \cos\theta \cos(kx - \omega t) - l_1 \sin\theta \sin(kx - \omega t) \\ l_2 \sin\theta \cos(kx - \omega t) + l_1 \cos\theta \sin(kx - \omega t) \end{pmatrix}. \end{aligned} \tag{23}$$

We recall that Eq. (1) describes the dimensional kinematics of the ciliary carpet as

$$\begin{pmatrix} x_s \\ y_s \end{pmatrix} = \begin{pmatrix} x + A\cos(kx - \omega t - \phi - kx_0) \\ B\sin(kx - \omega t - kx_0) \end{pmatrix}. \tag{24}$$

Hence, equating Eqs. (23) and (24) and expanding to separate the $\cos(kx - \omega t)$ and $\sin(kx - \omega t)$ terms yields

$$A\cos(kx_0 + \phi) = l_2 \cos\theta, \tag{25a}$$

$$A\sin(kx_0 + \phi) = -l_1 \sin\theta, \tag{25b}$$

$$B\cos kx_0 = l_1 \cos\theta, \tag{25c}$$

$$-B\sin kx_0 = l_2 \sin\theta. \tag{25d}$$

Eliminating x_0, these equations can be rearranged to give

$$\rho l = \cos\phi + l\tan\theta\sin\phi, \tag{26a}$$

$$-\rho\tan\theta = \sin\theta - l\tan\theta\cos\phi, \tag{26b}$$

TABLE I. Fitting cilia data to elliptical trajectories: estimations for the parameters $\{\theta_e, l_e\}$ and their corresponding uncertainties $\{\Delta\theta, \Delta l\}$ from experimental data for four different ciliated systems: *Volvox carteri* [48] and nasal cilia that are either healthy or diseased, caused by mutations in either the HYDIN or the DNAH11 protein [54].

Ciliated system	θ_e (°)	$\Delta\theta$ (°)	l_e	Δl
Volvox carteri [48]	73.7	10	0.443	0.2
Healthy nasal cilia [54]	45	10	0.5	0.2
HYDIN [54]	5.73	5	0.5	0.05
DNAH11 [54]	−45	10	0.5	0.2

where $l = l_2/l_1$ and $\rho = B/A = b/a = \sqrt{1-a^2}/a$. Hence, we can express (ρ, ϕ) in terms of (l, θ) through

$$\phi = \arctan\left(\frac{\tan\theta(l^2-1)}{l(1+\tan^2\theta)}\right), \tag{27a}$$

$$\rho = \tan\theta\sin\phi + \cos\phi/l. \tag{27b}$$

C. Experimental data

Obtaining estimates for l and θ from experimental data in the form $l = l_e \pm \Delta l$ and $\theta = \theta_e \pm \Delta\theta$, we can then use this mapping to get estimates for a and ϕ as a region of (a, ϕ) space for which $l(a, \phi)$ is in the interval $[l_e - \Delta l, l_e + \Delta l]$ and $\theta(a, \phi)$ is in the interval $[\theta_e - \Delta\theta, \theta_e + \Delta\theta]$.

In this paper, we consider four experimental systems for which data are available: two healthy ciliated carpets (*Volvox carteri* [48] and healthy nasal cilia [54]) and two diseased nasal ciliated systems (primary ciliary dyskinesia caused by mutations in either the HYDIN or the DNAH11 protein [54]). We have estimated $l = l_e \pm \Delta l$ and $\theta = \theta_e \pm \Delta\theta$ by taking graphical plots of the location of the center of mass of a cilia across a full stroke (Fig. 4(c) of Ref. [48] for the *Volvox carteri* cilium and Fig. 4(f) of Ref. [54] for the nasal cilia) and then fitting ellipses using the open-source image processing package fiji [55,56]. We state in Table I the resulting fits for the four experimental systems along with our estimated uncertainties.

D. Biological implications of stagnation regions

In Sec. IV, we identified theoretically that certain ciliary beating patterns can produce Lagrangian transport with zero, one, or two stagnation points. Here, we explore how these stagnation regions correlate with known health conditions, highlighting the biological relevance of our theoretical findings.

We postulate that the potential presence of stagnation regions may play a key biological role given the role of cilia in mucus clearance, for example, in the airways [9]. It is known that bacterial infection can alter the beating of cilia carpets [57,58], and thus if stagnation regions exist (i.e., regions with little flow), they could lead to increased residence time of bacteria and other suspended particles, resulting in clogging and increased bacterial infections.

How can we test this prediction quantitatively? We have already computed a full (a, ϕ) phase portrait in Fig. 4(b) showing the regions where stagnation points are present. By taking estimated values for a and ϕ from real biological systems, as carried out in Sec. V C, we can test whether healthy or unhealthy ciliary beating patterns correlate with no stagnation points or stagnation points, respectively.

These estimates for the regions in the model parameter space where real ciliated systems lie are superimposed onto Fig. 4, with green and yellow representing healthy and unhealthy cilia, respectively. Remarkably, both healthy cilia fall in white regions with no stagnation points, while both diseased cilia fall in red regions with one drift stagnation point. This suggests a potential relationship between the presence of drift stagnation points and the effectiveness of the ciliary beating pattern.

VI. CILIARY TRANSPORT OF ELONGATED PARTICLES

In the considerations above, we have focused on Lagrangian transport by ciliary flows of spherical particles (hence, we only needed to focus on the time evolution of their positions). However, in the case of nonspherical particles, the flow is also expected to change their orientations. In this section, for completeness we then extend our results to elongated particles. Specifically, we use Jeffery's classical equation [59] to characterize the dynamics of the orientation of an ellipsoidal particle in the flow created by the cilia carpet.

A. Model

For a flow of vorticity $\boldsymbol{\omega}$ and symmetric rate of strain tensor $\mathbf{E}$, the z component of the induced rate of rotation Ω of a prolate ellipsoid of aspect ratio r_e satisfies

$$\Omega = \frac{\omega_z}{2} + \frac{\tilde{B}\sin(2\theta)}{2}(E_{yy} - E_{xx}) + \tilde{B}\cos 2\theta E_{xy}, \tag{28}$$

where the shape factor of the particle $\tilde{B}$ is given by [59]

$$\tilde{B} = \left(\frac{r_e^2 - 1}{r_e^2 + 1}\right). \tag{29}$$

Given Eqs. (6) and (7), the rotational dynamics in Eq. (28) can be expanded to become

$$\begin{aligned}\frac{\partial\theta}{\partial t} = \Omega = {} & \epsilon b e^{-y}\sin(x-t) + \epsilon a e^{-y}\sin(x-t-\phi) \\ & + \epsilon\tilde{B}a e^{-y}(y-1)\sin(x-t-\phi+2\theta) \\ & + \epsilon\tilde{B}y b e^{-y}\sin(x-t+2\theta) + \epsilon^2 g_{\theta 1} + \mathcal{O}(\epsilon^3),\end{aligned} \tag{30}$$

where $g_{\theta 1}$ is $\mathcal{O}(1)$ and 2π periodic in t.

B. Trajectories from multiple-scale analysis

Since the orientation of the passive particle is decoupled from its position, we can now employ a similar multiple-scale approach to characterize the time evolution of the orientation. Expressing θ as a function of t and $T = \epsilon^2 t$, we expand θ as a series expansion in powers of ϵ, i.e.,

$$\theta = \theta_0 + \epsilon\theta_1 + \epsilon^2\theta_2 + \cdots. \tag{31}$$

At $\mathcal{O}(1)$, Eq. (30) becomes

$$\frac{\partial \theta_0}{\partial t} = 0, \tag{32}$$

i.e., as expected θ_0 is also only a function of T.

At $\mathcal{O}(\epsilon)$, taking Eq. (30) and integrating with respect to t yields

$$\begin{aligned}\theta_1 = {} & be^{-y_0}\cos(x_0 - t) + ae^{-y_0}\cos(x_0 - t - \phi) \\ & + \tilde{B}ae^{-y_0}(y_0 - 1)\cos(x_0 - t - \phi + 2\theta_0) \\ & + \tilde{B}y_0 be^{-y_0}\cos(x_0 - t + 2\theta_0) + g_{\theta 2}(T),\end{aligned} \tag{33}$$

where $g_{\theta 2}$ is independent of t, i.e., just a function of T.

At $\mathcal{O}(\epsilon^2)$, Eq. (30) becomes

$$\begin{aligned}&\frac{\partial \theta_2}{\partial t} + \frac{\partial \theta_0}{\partial T} \\ &= -by_1 e^{-y_0}\sin(x_0 - t) \\ &\quad + bx_1 e^{-y_0}\cos(x_0 - t) - ay_1 e^{-y_0}\sin(x_0 - t - \phi) \\ &\quad + ax_1 e^{-y_0}\cos(x_0 - t - \phi) \\ &\quad + \tilde{B}by_1(1 - y_0)e^{-y_0}\sin(x_0 - t + 2\theta_0) \\ &\quad + \tilde{B}by_0(x_1 + 2\theta_1)e^{-y_0}\cos(x_0 - t + 2\theta_0) \\ &\quad + \tilde{B}a(y_0 - 1)(x_1 + 2\theta_1)e^{-y_0}\cos(x_0 - t + 2\theta_0 - \phi) \\ &\quad + \tilde{B}ay_1(2 - y_0)e^{-y_0}\sin(x_0 - t - \phi + 2\theta_0) + g_{\theta 1}.\end{aligned} \tag{34}$$

As above, assuming periodicity in a 2π interval of t of θ_2 and integrating between 0 and 2π with respect to t gives

$$\begin{aligned}\frac{\partial \theta_0}{\partial T} = {} & \frac{a^2 e^{-2y_0}}{2}\left(1 - 2y_0 + \tilde{B}\cos 2\theta_0\left(6y_0 - 3 - 2y_0^2\right)\right. \\ & \left. + 2\tilde{B}^2(1 - y_0)^2\right) + \frac{b^2 e^{-2y_0}}{2}\left(-1 - 2y_0\right. \\ & \left. + \tilde{B}\cos 2\theta_0\left(2y_0 + 1 - 2y_0^2\right) + 2\tilde{B}^2 y_0^2\right) \\ & + 2aby_0 e^{-2y_0}\cos\phi\left(-1 + \tilde{B}\cos 2\theta_0(2 - y_0)\right. \\ & \left. + \tilde{B}^2(y_0 - 1)\right).\end{aligned} \tag{35}$$

C. Comparison with numerical results

Following the approach applied above for spatial position (x, y), we compare in Fig. 6 the numerical solutions of Eq. (33) (solid curves) with asymptotic approximations for the drift obtained from Eq. (35) (dashed curves), plotting θ as a function of time t for a range of values for $(\theta(0), \phi, \tilde{B})$ with $a = b = 1/\sqrt{2}$, $x(0) = 0$, $y(0) = 0.3$, and $\epsilon = 0.05$. Darker blue indicates smaller $\theta(0)$.

Inspecting in particular the insets of Fig. 6, and similarly to the particle position in Fig. 2, we obtain very good agreement between theoretical predictions and the numerical results. The dynamics in Fig. 6(a) is representative of the results for near-spherical particles ($\tilde{B} = 0.2$). Since all θ_0 dependence in Eq. (35) is $\mathcal{O}(\tilde{B})$ with respect to $\tilde{B}$, a small value of $\tilde{B}$ leads to the leading-order contribution to the Lagrangian drift being independent of θ, i.e., straight lines. Furthermore, as can be seen in the inset of Fig. 6(a), the amplitude of the oscillatory terms is also independent of θ.

In contrast, for more elongated particles where $\tilde{B}$ is larger [see Figs. 6(b) and 6(c), in the case $\tilde{B} = 0.8$], the drift becomes nonlinear in θ_0. Depending on where we are in the $(a, \phi, y(0))$ phase space, we approach either a limit cycle [see Fig. 6(b) where all gradients are negative] or a stagnation point [see Fig. 6(c) where the gradients are both positive and negative]. The insets of Figs. 6(b) and 6(c) also clearly convey that the the amplitude of oscillation varies nonlinearly with θ_0.

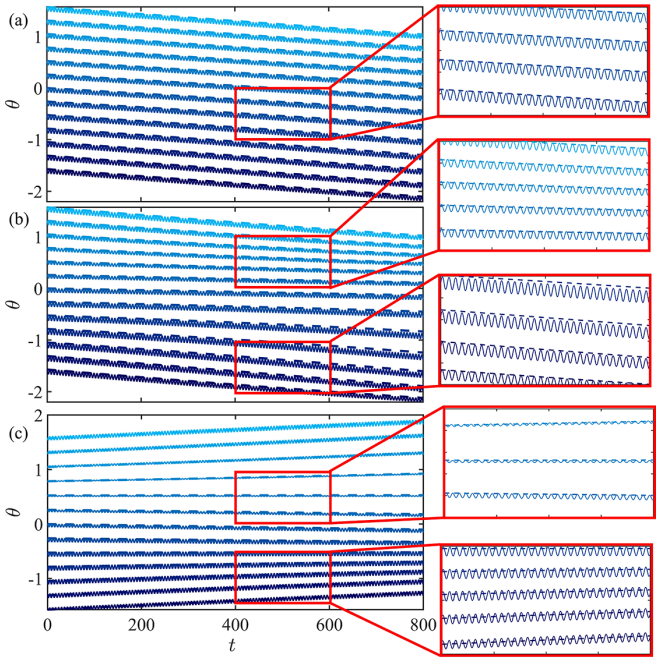

FIG. 6. Lagrangian trajectories of the orientation of elongated particles: numerical solutions (solid curves) and asymptotic approximations for the drift (dashed curves), plotting θ as a function of time t for $\theta(0) \in (-\pi/2, -5\pi/12, -\pi/3, -\pi/4, -\pi/6, -\pi/12, 0, \pi/12, \pi/6, \pi/4, \pi/3, 5\pi/12, \pi/2)$ and a range of values for $(\phi, \tilde{B})$ with $a = 1/\sqrt{2}$, $x(0) = 0$, $y(0) = 0.3$, and $\epsilon = 0.05$. Darker blue indicates smaller $\theta(0)$. (a) $\phi = \pi/3$, $\tilde{B} = 0.2$. (b) $\phi = \pi/3$, $\tilde{B} = 0.8$. (c) $\phi = 2\pi/3$, $\tilde{B} = 0.8$. Insets provide enlarged views.

VII. CONCLUSIONS

In summary, motivated by the desire to understand transport by ciliary arrays, we have shown theoretically and computationally that the classical Eulerian view on cilia-induced flow misses a key aspect of time-averaged Lagrangian transport. Specifically, using Taylor's classical waving model, we exploited the separation of timescales between the fast periodic trajectories and the slower time horizontal drift and uncovered that the time-averaged drift generated by the time-varying motion of the cilia is not uniform (as predicted by classical studies) but instead varies with the distance from the ciliary surface, in a nonmonotonic way. This result reveals a rich set of transport behaviors, including flow recirculation and drift stagnation points.

In particular, the existence of stagnation points was shown to correlate with two known types of unhealthy cilia tissues, potentially providing a way to distinguish healthy from impaired ciliary beating patterns. This correlation was demonstrated using a reduced elliptical model to capture the motion

of a single cilium and map experimental ciliary trajectories to the corresponding Taylor's beating sheet parameter values (a, ϕ). Further work will be required to fully evaluate the validity of this ellipse approximation, particularly for unhealthy ciliary beating patterns.

A logical next step will be to build on this framework by adding biological complexity, for example, by considering more realistic, nonsmooth waving shapes for the cilia envelope [60] or by coupling the cilia-induced flow with the swimming of flagellated bacteria [6]. The multiple-scale approach used here will also be applicable beyond cilia-induced flow to other systems driven by oscillatory deformation, such as peristaltic pumping [28,29].

ACKNOWLEDGMENTS

We thank our colleague Ray Goldstein for the use of his laboratory in order to produce the image in Fig. 1. We thank the group of Pietro Cicuta, in particular Erika Causa and Viridiana Sosa, for extensive discussions including demonstrations of their experiments tracking ciliary beating patterns. We also thank our colleagues Ray Goldstein and Tim Pedley for useful discussions on modeling ciliated arrays. This work was supported by EPSRC Grant No. EP/W024012/1.

DATA AVAILABILITY

No data were created or analyzed in this study.

[1] N. Klena and G. Pigino, Structural biology of cilia and intraflagellar transport, Annu. Rev. Cell Dev. Biol. **38**, 100 (2022).

[2] C. Brennen and H. Winet, Fluid mechanics of propulsion by cilia and flagella, Annu. Rev. Fluid Mech. **9**, 339 (1977).

[3] J. Blake, Fluid mechanics of cilliary propulsion, in *Computational Modeling in Biological Fluid Mechanics*, edited by L. J. Fauci and S. Gueron (IMA, New York, USA, 2001), Vol. 124, pp. 1–51.

[4] D. J. Smith, E. A. Gaffney, and J. R. Blake, Mathematical of cilia-driven transport of biological fluids, Proc. R. Soc. A. **465**, 2417 (2009).

[5] S. Childress, *Mechanics of Swimming and Flying* (Cambridge University Press, Cambridge, 1981).

[6] E. Lauga, *The Fluid Dynamics of Cell Motility* (Cambridge University Press, Cambridge, 2020).

[7] G. T. Fortune, A. Worley, A. B. Sendova-Franks, N. R. Franks, K. C. Leptos, E. Lauga, and R. E. Goldstein, The fluid dynamics of collective vortex structures of plant-animal worms, J. Fluid Mech. **914**, A20 (2021).

[8] J. R. Velez-Cordero and E. Lauga, Waving transport and propulsion in a generalized Newtonian fluid, J. Non-Newtonian Fluid Mech. **199**, 37 (2013).

[9] D. J. Smith, E. A. Gaffney, and J. R. Black, Modelling mucociliary clearance, Respir. Physiol. Neurobiol. **163**, 178 (2008).

[10] G. R. Fulford and J. R. Blake, Muco-ciliary transport in the lung, J. Theor. Biol. **121**, 381 (1986).

[11] L. J. Fauci and R. Dillon, Biofluidmechanics of reproduction, Annu. Rev. Fluid Mech. **38**, 371 (2006).

[12] T. J. Lardner and W. J. Shack, Cilia transport, Bull. Math. Biophys. **34**, 325 (1972).

[13] C. O'Callaghan, K. Sikand, and M. A. Chilvers, Analysis of ependymal ciliary beat pattern and beat frequency using high speed imaging: Comparison with the photomultiplier and photodiode methods, Cilia **1**, 8 (2012).

[14] I. Ibañez-Tallon, N. Heintz, and H. Omran, To beat or not to beat: Roles of cilia in development and disease, Hum. Mol. Genet. **12**, 27R (2003).

[15] G. I. Taylor, Analysis of the swimming of microscopic organisms, Proc. R. Soc. A **209**, 447 (1951).

[16] J. R. Blake, Infinite models for ciliary propulsion, J. Fluid Mech. **49**, 209 (1971).

[17] J. E. Drummond, Propulsion by oscillating sheets and tubes in a viscous fluid, J. Fluid Mech. **25**, 787 (1966).

[18] A. J. Reynolds, The swimming of minute organisms, J. Fluid Mech. **23**, 241 (1965).

[19] E. O. Tuck, A note on a swimming problem, J. Fluid Mech. **31**, 305 (1968).

[20] S. Childress, Inertial swimming as a singular perturbation, in *Proceedings of the ASME 2008 Dynamic Systems and Control Conference* (ASME, New York, USA, 2008), pp. 1413–1420.

[21] T. Y. T. Wu, Swimming of a waving plate, J. Fluid Mech. **10**, 321 (1961).

[22] T. Y. T. Wu, Hydrodynamics of swimming propulsion. Part I. Swimming of a two-dimensional flexible plate at variable speeds in an inviscid fluid, J. Fluid Mech. **46**, 337 (1971).

[23] G. I. Taylor, The action of waving cylindrical tails in propelling microscopic organisms, Proc. R. Soc. A **211**, 225 (1952).

[24] T. K. Chaudhury, On swimming in a visco-elastic liquid, J. Fluid Mech. **95**, 189 (1979).

[25] L. D. Sturges, Motion induced by a waving plate, J. Non-Newtonian Fluid Mech. **8**, 357 (1981).

[26] G. R. Fulford, D. F. Katz, and R. L. Powell, Swimming of spermatozoa in a linear viscoelastic fluid, Biorheology **35**, 295 (1998).

[27] E. Lauga, Propulsion in a viscoelastic fluid, Phys. Fluids **19**, 083104 (2007)

[28] A. H. Shapiro, M. Y. Jaffrin, and S. L. Weinberg, Peristaltic pumping with long wavelengths at low Reynolds number, J. Fluid Mech. **37**, 799 (1969).

[29] M. Y. Jaffrin and A. H. Shapiro, Peristaltic pumping, Annu. Rev. Fluid Mech. **3**, 13 (1971).

[30] C. Brennen, Oscillating boundary layer for ciliary propulsion, J. Fluid Mech. **65**, 799 (1974).

[31] T. Ishikawa, Fluid dynamics of squirmers and ciliated microorganisms, Annu. Rev. Fluid Mech. **56**, 119 (2024).

[32] H. Guo, H. Zhu, R. Liu, M. Bonnet, and S. Veerapaneni, Optimal ciliary locomotion of axisymmetric microswimmers, J. Fluid Mech. **927**, A22 (2021).

[33] T. Omori, H. Ito, and T. Ishikawa, Swimming microorganisms acquire optimal efficiency with multiple cilia, Proc. Natl. Acad. Sci. USA **117**, 30201 (2020).

[34] T. Nguyen, Y. Koga, T. Wakasugi, T. Kitamura, and H. Suzuki, Nasal polyps show decreased mucociliary transport despite vigorous ciliary beating, Braz. J. Otorhinolaryngol. **90**, 101377 (2024).

[35] D. Palazzolo, J. M. Nelson, E. Ely, A. Crow, J. Distin, and S. Kunigelis, The effects of electronic cigarette (ECIG)-generated aerosol and conventional cigarette smoke on the mucociliary transport velocity (MTV) using the bullfrog (*R. catesbiana*) palate paradigm, Front. Physiol. **8**, 1023 (2017).

[36] G. Schmidt, F. Borchers, S. Müller, A. Akbari, F. Edinger, M. Sander, C. Koch, and M. Henrich, Dobutamine, epinephrine, and milrinone accelerate particle transport velocity in murine tracheal epithelium via Ca^{2+} release from caffeine-sensitive internal stores, Cells, **14**, 228 (2025).

[37] S. Kelly, P. Martinsen, and S. Tatkov, Rapid changes in mucociliary transport in the tracheal epithelium caused by unconditioned room air or nebulized hypertonic saline and mannitol are not determined by frequency of beating cilia, ICMx, **9**, 8 (2021).

[38] The MathWorks, Inc., *MATLAB and Image Processing Toolbox Release 2023b* (The MathWorks Inc., Natick, MA, 2023).

[39] E. J. Hinch, *Perturbation Methods* (Cambridge University Press, Cambridge, 1991).

[40] B. van der Pol, A theory of the amplitude of free and forced triode vibrations, Radio Rev. **1**, 701 (1920).

[41] A. A. Dorodnicyn, Asymptotic solution of Van der Pol's equation, Prikl. Mat. Mekh. **11**, 313 (1947).

[42] K. Ma, N. Pujara, and J.-L. Thiffeault, Reaching for the surface: Spheroidal microswimmers in surface gravity waves, Phys. Rev. Fluids **7**, 014310 (2022).

[43] E. A. Gaffney, M. P. Dalwadi, C. Moreau, K. Ishimoto, and B. J. Walker, Canonical orbits for rapidly deforming planar microswimmers in shear flow, Phys. Rev. Fluids **7**, L022101 (2022).

[44] B. J. Walker, K. Ishimoto, E. A. Gaffney, C. Moreau, and M. P. Dalwadi, Effects of rapid yawing on simple swimmer models and planar Jeffery's orbits, Phys. Rev. Fluids **7**, 023101 (2022).

[45] B. J. Walker, K. Ishimoto, and E. A. Gaffney, Systematic of minimal models of microswimming, Phys. Rev. Fluids **8**, 034102 (2023).

[46] M. P. Dalwadi, C. Moreau, E. A. Gaffney, K. Ishimoto, and B. J. Walker, Generalised Jeffery's equations for rapidly spinning particles. Part 1: Spheroids, J. Fluid Mech. **979**, A1 (2024).

[47] E. A. Gaffney, K. Ishimoto, and B. J. Walker, Motility and rotation of multi-timescale microswimmers in linear background flows, J. Fluid Mech. **1022**, A13 (2025).

[48] D. R. Brumley, K. Y. Wan, M. Polin, and R. E. Goldstein, Flagellar synchronization through direct hydrodynamic interactions, eLife **3**, e02750 (2014).

[49] T. Niedermayer, B. Eckhardt, and P. Lenz, Synchronization, phase locking, and metachronal wave formation in ciliary chains, Chaos **18**, 037128 (2008).

[50] N. Uchida and R. Golestanian, Generic conditions for hydrodynamic synchronization, Phys. Rev. Lett. **106**, 058104 (2011).

[51] N. Uchida and R. Golestanian, Hydrodynamic synchronization between objects with cyclic rigid trajectories, Eur. Phys. J. E **35**, 135 (2012).

[52] F. Boselli, J. Jullien, E. Lauga, and R. Goldstein, Fluid mechanics of mosaic ciliated tissues, Phys. Rev. Lett. **127**, 198102 (2021).

[53] W. Wang, I. Tanasijevic, J. Zhang, E. Lauga, and I. Cohen, Electronically actuated artificial hinged cilia for efficient bidirectional pumping, Lab Chip **24**, 4549 (2024).

[54] M. Chioccioli, L. Feriani, Q. Nguyen, J. Kotar, S. D. Dell, V. Mennella, I. Amirav, and P. Cicuta, A how-to guide to: Quantitative high-speed video profiling to discriminate between variants of primary ciliary dyskinesia, bioRxiv, https://doi.org/10.1101/614966.

[55] C. A. Schneider, W. S. Rasband, and K. W. Eliceiri, NIH Image to ImageJ: 25 years of image analysis, Nat. Methods **9**, 671 (2012).

[56] J. Schindelin, I. Arganda-Carreras, E. Frise, V. Kaynig, M. Longair, T. Pietzsch, S. Preibisch, C. Rueden, S. Saalfeld, B. Schmid, J.-Y. Tinevez, D. J. White, V. Hartenstein, K. Eliceiri, P. Tomancak, and A. Cardona, Fiji: an open-source platform for biological-image analysis, Nat. Methods **9**, 676 (2012).

[57] M. Mewe, D. Tielker, R. Schönberg, M. Schachner, K.-E. Jaeger, and U. Schumacher, *Pseudomonas aeruginosa* lectins I and II and their interaction with human airway cilia, J. Laryngol. Otol. **119**, 595 (2005).

[58] J. Galli, L. Calò, F. Ardito, M. Imperiali, E. Bassotti, G. C. Passali, G. La Torre, G. Paludetti, and G. Fadda, Damage to ciliated epithelium in chronic rhinosinusitis: What is the role of bacterial biofilms? Ann. Otol. Rhinol. Laryngol **117**, 902 (2008).

[59] G. B. Jeffery, The motion of ellipsoidal particles immersed in a viscous fluid, Proc. R. Soc. A. **102**, 161 (1922).

[60] T. D. Montenegro-Johnson and E. Lauga, Optimal swimming of a sheet, Phys. Rev. E **89**, 060701(R) (2014).